Chinese Chemical Letters 37 (2026) 112071

Contents lists available at ScienceDirect

Chinese Chemical Letters

journal homepage: www.elsevier.com/locate/cclet

Dissolved microneedle loading polydopamine nanoparticles induced tumor-associated macrophage polarization and promoted dendritic cell maturation for tumor immunotherapy

Ping Sun[a], Nansha Gao[b,c,*], Li Yang[a], Yao Yang[a], Li Huang[a], Hongzhong Chen[a], Hualin Ma[d,*], Xiaowei Zeng[a,*]

[a] School of Pharmaceutical Sciences (Shenzhen), Shenzhen Campus of Sun Yat-sen University, Shenzhen 518107, China
[b] Guangzhou Vocational University of Science and Technology, Guangzhou 510550, China
[c] Shenzhen Children's Hospital, Clinical Medical College of Southern University of Science and Technology, Shenzhen 518038, China
[d] Shenzhen key Laboratory of Kidney Diseases, Department of Nephrology, Shenzhen People's Hospital, (The Second Clinical Medical College, Jinan University; The First Affiliated Hospital, Southern University of Science and Technology), Shenzhen 518020, China

ARTICLE INFO

Article history:
Received 19 August 2025
Revised 3 November 2025
Accepted 5 November 2025
Available online 5 November 2025

Keywords:
Dissolving microneedles
Tams polarization
Dendritic cell activation
Transdermal delivery
Tumor immunotherapy

ABSTRACT

Microneedles (MNs) represent a rapidly evolving transdermal drug delivery method, with ongoing development efforts focused on overcoming challenges such as limited drug loading and pore occlusion. Herein, we report dissolvable MNs vaccine with excellent drug loading as well as other positive features that make it an ideal delivery carrier in tumor immunotherapy. This study employs a biodegradable polydopamine-based nano-delivery system to co-encapsulate both Toll-like receptor 7/8 agonist resiquimod (R848) and ovalbumin (OVA) antigens, which are subsequently incorporated into MN patches to achieve synergistic photothermal-immunotherapeutic effects. The MN vaccine targets tumor sites via transdermal administration, exhibiting significant therapeutic efficacy by enabling deep tissue drug release and maintaining prolonged therapeutic levels for at least 3 days. The MN tips are rapidly degraded under photothermal action to release R848 and OVA, can effectively polarizes the tumor-associated macrophages to M1-type macrophages and activate dendritic cells to enhance immune response *in vivo*, thereby, the MN vaccines have shown excellent efficacy and good safety, resulting in a sufficient and persistent anti-tumor cellular immune response with potent tumor immunotherapeutic efficacy. In brief, this study demonstrates that MN administration successfully delivers polydopamine-based nanotherapeutics to tumor sites and validates their anti-tumor efficacy.

© 2026 Published by Elsevier B.V. on behalf of Chinese Chemical Society and Institute of Materia Medica, Chinese Academy of Medical Sciences.

Microneedles (MNs) were first introduced in the late 1990s as a delivery system for the percutaneous administration directly into the dermis to produce both local and systemic pharmacological effects [1]. The MNs create pathways by puncturing the stratum corneum, allowing drug molecules to diffuse beneath the skin much more rapidly. This technology has enabled the transdermal delivery of complex molecules such as proteins, vaccines, and peptides. The MNs can be classified into various types, including solid, hollow, coated, and dissolving, all were designed to facilitate rapid and efficient drug delivery [2,3]. The use of MN array patches (MAPs) for vaccination, particularly in the therapy of tumors, has shown as a promising trend in the pharmaceutical industry [4,5]. MAPs offer several advantages, such as enhanced stability, efficient delivery, room-temperature storage, painless application, minimal invasiveness and intradermal delivery of antigens into the skin. These MAPs are designed to deliver vaccines into the epidermal and dermal layers, which house Langerhans and dendritic cells (DCs) crucial for immune responses. The MNs in MAPs typically range from 100 μm to 1000 μm in length. Three types of solid-MAPs, coated-MAPs and dissolving-MAPs have been developed and tested for immunization applications. The solid-MAPs deliver vaccines into deeper skin layers through the channels created by the MNs. The coated-MAPs directly release the vaccine formulation into the skin upon insertion, ensuring immediate delivery. The dissolving-MAPs are composed of safe, inert, water-soluble materials, and release the vaccine from the MNs matrix after insertion into the skin. The application of MAPs in tumor prevention

* Corresponding authors.
E-mail addresses: gaonansha_1@163.com (N. Gao), mahualin0796@sina.com (H. Ma), zengxw23@mail.sysu.edu.cn (X. Zeng).

https://doi.org/10.1016/j.cclet.2025.112071
1001-8417/© 2026 Published by Elsevier B.V. on behalf of Chinese Chemical Society and Institute of Materia Medica, Chinese Academy of Medical Sciences.

and treatment represents a significant advancement in the field of medicine, highlighting their potential for innovative drug and vaccine delivery systems [6–8].

Immunotherapy has become an effective strategy for treating cancer, utilizing the role of immune cells in the tumor microenvironment. Despite its clinical success in the treatment of various cancer types, immunotherapy still has its disadvantages that need to be overcome, for instance, checkpoint blockade therapy, while effective for some patients, is associated with severe systemic side effect and is beneficial only for tumors in the appropriate immunological state. The engagement of Toll-like receptors (TLRs), coupled with the inhibition of tumor-promoting immune signaling, offers a promising therapeutic avenue for advancing immunotherapy through modulation of the tumor microenvironment [9–11]. The TLRs is mainly expressed by immune cells, and TLR-7 is an endosomal single stranded RNA receptor mainly expressed by macrophages, plasmacytoid DCs, natural killer cells, and B cells. Ruiquimod (R848) is a immunomodulatory agent belonging to the TLR-7/8 agonist family, after binding to TLR-7/8, R848 induces the release of various immune regulatory cytokines, including interleukin-6 (IL-6), IL-12, and tumor necrosis factor-alpha (TNF-α), the release of this cytokine triggers a series of signaling pathways, activating antigen-presenting cells (APCs) and polarizing T cell responses [12–14]. Although the role of TLRs in inducing innate immune responses against bacterial and viral pathogens has been extensively studied, their role in anti-cancer immune monitoring has only recently received attention. The TLR-7/8 signaling promotes anti-cancer response by activating central transcription factor nuclear factor-kappa B (NF-κB) [15]. Additionally, the TLR-7/8 therapy was found to expand tumor antigen specific $CD8^+$ T cells that are critical to develop effective anti-tumor immune responses [16,17].

Photothermal therapy (PTT) is a potential tumor treatment strategy, which employs heat and light energy to obliterate tumor cells selectively. This treatment strategy has attracted extensive attention and is the focus of extensive investigation for its therapeutic potential in tumor therapy. Advances in photothermal conversion agents including of mesoporous polydopamine (MPDA), carbon nanotubes and gold nanoparticles (NPs), have demonstrated remarkable efficacy in absorbing light energy under near-infrared (NIR) light exposure [18–21]. This treatment strategy is a promising approach to effectively and minimally invasively ablate tumor tissue by increasing the heat at the tumor site. Although PTT is presented potential tumor inhibition in various investigation. There is inevitable challenge, for example, when mediated tumor cell injury, PTT can induce the release of intracellular components from tumor tissue into the extracellular environment, triggering a series of inflammatory reactions. This cascade reaction typically involves the production of inflammatory factors such as IL-1β, TNF-α and IL-6, which then activate survival genes within residual cancer cells and increase the risk of cancer recurrence [22]. To overcome these defects, many scientists have begun pioneering research combining PTT with immunotherapy method [23,24]. This comprehensive treatment strategy aims to alleviate the immune response associated with PTT for improving its therapeutic efficacy and lowering the risk of tumor recurrence.

Multifunctional MPDA NPs have the advantages of simple synthesis process and good biocompatibility, and have therefore received widespread attention. The MPDA NP possess inherent properties such as exceptional photothermal characteristics and robust free radical scavenging ability. Numerous studies have demonstrated their efficacy in facilitating tumor tissue ablation under NIR light irradiation [25,26]. Adding MPDA to this design provides critical advantages, including enhanced intracellular protein delivery, improved photothermal conversion efficiency, and free radical scavenging capabilities [27]. Additionally, a large and uniform

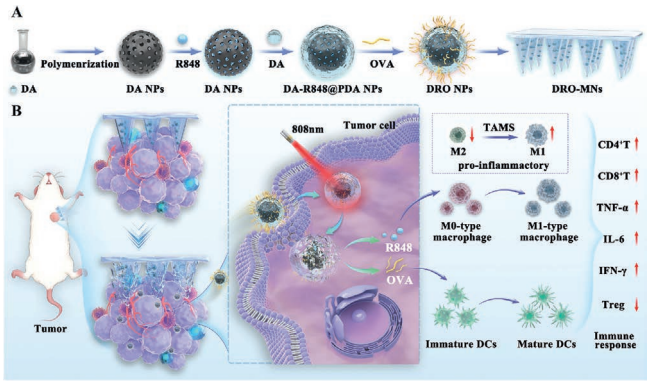


Fig. 1. Schematic illustration of DRO-MNs preparation and induced tumor-associated macrophage polarization and DCs maturation for tumor immunotherapy.

number of holes on MPDA NPs provide appropriately sized cavities and broad surface area for containing protein payload. Polydopamine (PDA) holds a wide absorption spectrum in the NIR spectral ranges, this feature can achieve photothermal conversion in cancer treatment, which, under NIR irradiation, facilitates the controlled release of anchored proteins through disrupting the non-covalent coordination bonds between PDA and metal ions. In addition, as the first perimeter of withstand bacterial infections, macrophage recognizes various pathogens by expressing receptors that bind to microbial molecular patterns, most eye-catching TLRs complexes. Therefore, exploiting macrophage membranes pretreated with microbes to induce the expression of corresponding TLRs offers a viable approach for targeted delivery. The application of macrophage membrane coatings for targeted therapy of bacterial infections has also been proved. These excellent features enable effective drug delivery and enhance the inhibitory effect on cancer, making MPDA a promising candidate for anti-tumor PTT [28,29].

In this study, we demonstrate the enormous potential of dissolving MN for delivering MPDA NPs to stimulate concurrent innate and adaptive immune response for tumor immunotherapy. First, these PDA NPs were prepared to encapsulate R848 and OVA for improving encapsulation efficiency and overcoming hydrophilicity, and the drug-loaded PDA NPs were then incorporated into the body of the dissolving MN. This MN was employed for transdermal delivery in tumor-bearing mice, where it exhibited high uptake efficiency, effectively polarized tumor-associated macrophages, and promoted the maturation of DCs. In contrast to dopamine NPs, which mediate immunotherapeutic effects through immunogenic cell death (ICD), ovalbumin (OVA) acts by activating the maturation of DCs. Additionally, this approach reversed the immunosuppressive of tumor microenvironment and enhanced T cell responses under NIR irradiation (Fig. 1). We further evaluated the efficacy of this strategy in both preventive and therapeutic environments using a mouse allogeneic tumor transplantation model, the results demonstrated that MN-mediated delivery of PDA NPs markedly enhanced their anti-tumor efficacy *in vivo*.

This study constructed a porous dopamine NPs through a multistep polymerization reaction. The R848 was placed in the surface hole of the nano-system, after which this nano-system was coated with a PDA layer using an *in-situ* polymerization method to prepare DA-R848 NPs (DR NPs). OVA was conjugated to the surface of the DA-coated layer through a Michael addition reaction, forming a nano-platform that co-loads R848 and OVA.

Evaluation for the basic properties of DR NPs and DRO NPs, and the research result was display in Fig. 2. The average particle size of DR NPs is about 200 nm (Fig. 2A). In comparison, the average particle size of DRO NPs was about 220 nm, indicating that OVA-modified NPs were slightly larger than their non- modified coun-

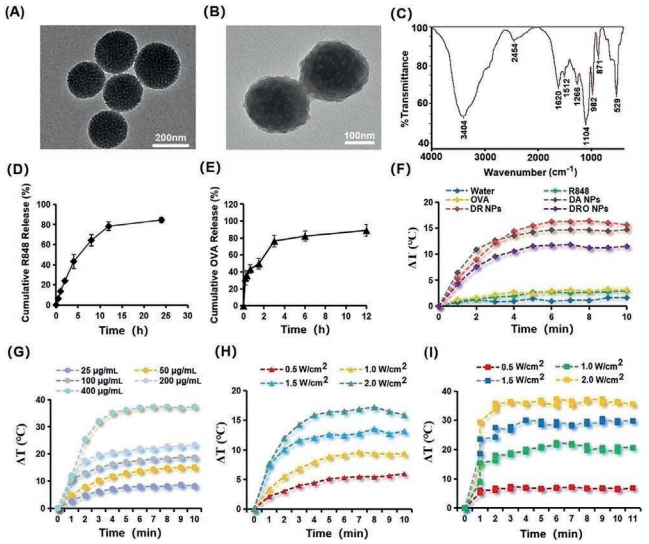


Fig. 2. Preparation and characterization of DRO NPs. (A) The TEM images of DR NPs. (B) The TEM images of DRO NPs. (C) The FTIR spectra of DRO NPs. (D) Release profiles of R848 from DRO NPs for 24 h in PBS. (E) Release profiles of OVA from DRO NPs for 12 h in PBS. (F) Temperature elevation curves of water, R848, OVA, DA NPs, DR NPs and DRO NPs under 808 nm laser irradiation (1.0 W/cm^2) for 5 min. (G) Photothermal heating curves of the DRO NPs for different concentration and being irradiated with the 808 nm laser (1.0 W/cm^2) for 5 min. (H) Photothermal heating curves of the DRO NPs for different power being irradiated with the 808 nm laser. (I) Photothermal heating curves of DRO-MNs for different power being irradiated with the 808 nm laser. Data are shown as mean ± SD ($n = 3$).

terparts. The surface morphology of DRO NPs showed uniform particle size distribution (Fig. 2B).

Fourier transform infrared (FTIR) spectroscopy was employed to confirm the structure of DRO NPs. In the FTIR spectrum (Fig. 2C and Fig. S1 in Supporting information), the broad peak at 3400 cm^{-1} originates from the stretching vibration of the phenolic hydroxyl group in molecular structure of dopamine, and the characteristic peaks of R848 were observed within the wavelength range of 1104 cm^{-1}, it originates from the stretching vibration of C–O-C of aliphatic ether, while the characteristic peaks of OVA were observed at wavelengths of 1620 and 1512 cm^{-1}, it originates from the stretching vibration of C=O (amide I band) and C–N (amide II band) respectively, the results verified the successful construction of DRO NPs [30].

The cumulative release study results for R848 and OVA indicated that the release rate of DRO NPs significantly increased with NIR light exposure. After 24 h of R848 release, approximately 80 % of DRO NPs were released under light radiation (Fig. 2D). Meanwhile, the cumulative release of OVA reached 83 % after 12 h (Fig. 2E), demonstrating that the release of R848 and OVA from DRO NPs is significantly influenced by light.

Temperature variations of water, R848, OVA, DA NPs, DR NPs, and DRO NPs (100 μg/mL) were measured under NIR laser radiation for 5 min at 1.0 W/cm^2, as shown in Fig. 2F. Almost no photothermal absorption was observed in the water, R848, and OVA groups. However, after the dopamine layer was applied, the temperatures of DA NPs, DR NPs and DRO NPs rised significantly, with the temperature of DRO NPs rising by nearly 10–15 °C. In contrast, the temperature of ultra-pure water increased by only 2 °C under the same conditions. These results confirm that DA NPs possess good photothermal properties. The photothermal properties of DRO NPs, modified by OVA, exhibited no significant difference from those of DA NPs, indicating that DRO NPs meet the requirements for tumor ablation through photothermal effects. The photothermal effect of DRO NPs is concentration- dependent, with temperature rises with concentrations increasing (Fig. 2G). Additionally,

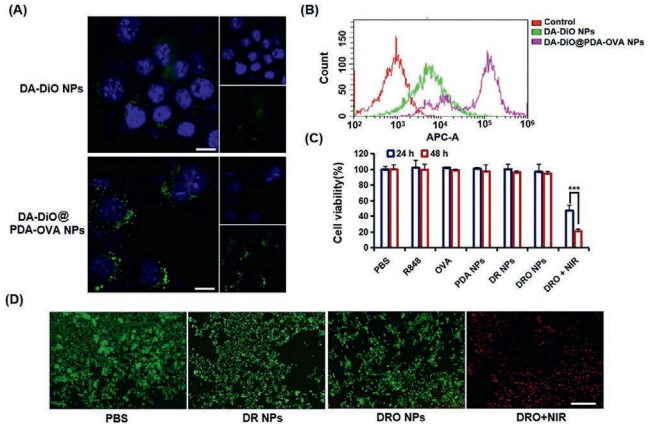


Fig. 3. Extracellular absorbance profiles of different type NP. (A) CLSM images of 4T1 cells after incubation with DA-DiO NPs and DA-DiO@PDA-OVA NPs for 4 h, scale bar: 10 μm. (B) Flow cytometry detection of DA-DiO NPs and DA-DiO@PDA-OVA NPs in PBS. (C) Cell viability of 4T1 cells treated with different NP with and without NIR irradiation for 24 or 48 h. Data are shown as mean ± SD ($n = 5$). $^{***}P < 0.001$. (D) The live/dead staining images of 4T1 cells under various treatments models, viable cells were stained green with calcein-AM, and dead/late apoptosis cells were stained red with propidium iodide (PI). Scale bar: 10 μm.

DRO NPs showed an increased temperature rise with elevated laser power density (Fig. 2H). Furthermore, the photothermal properties of the MN loaded with DRO NPs were investigated at varying laser power densities, the results showed that as laser power density increased, the temperature of the MN significantly rose, indicating that the MN loaded with DRO NPs possesses good photothermal performance and can be used for the PTT of tumors (Fig. 2I)

The 4T1 cells were co-incubated with different nanoplatform under the same conditions for 4 h. The laser scanning confocal microscope (LSCM) was then utilized for visualizing the fluorescence staining of the nanoplatform and nuclei. This approach allowed for the evaluation of their extracellular absorption performance. The nuclei were stained using 4′,6-diamidino-2-phenylindole fluorescence, while DA-DiO NPs and DA-DiO@PDA-OVA NPs were detected using the green fluorescence they generated. The result was presented in Fig. 3. It is evident that the DA-DiO@ PDA-OVA NPs group exhibits the strongest green fluorescence surrounding the cell nuclei compared to the DA-DiO NPs group in phosphate buffered saline (PBS) (Fig. 3A). This observation indicates that, following co-incubation with tumor cells, DA-DiO@ PDA-OVA NPs can effectively mediate the absorption by tumor cells, thereby enhance the entry of nanoplatform into the cells. This conclusion was further corroborated by flow cytometry analysis (Fig. 3B), providing evidence for the increased absorption of DA-DiO@PDA-OVA NPs by tumor cells.

Cell viability following incubation with different types of NPs was assessed using the cell counting kit-8 method. The experimental results are shown in Fig. 3C. The growth inhibition of 4T1 cells was investigated after administering PBS, R848, OVA, DA NPs, DR NPs, DRO NPs, and DRO+NIR for 24 and 48 h, respectively. Except for the DRO+NIR group, all other groups exhibited good cell viability and showed no growth inhibition. Cell proliferation was significantly inhibited after exposure to NIR with a wavelength of 808 nm for 5 min, further underscoring the importance of the photothermal effect on tumor cell growth.

A cell live/dead staining kit was employed in this study to estimate cell cytotoxicity. The research result was illustrated in Fig. 3D, and the highest proportion of dead cells were observed in DRO+NIR group, while the other groups displayed healthy cell growth without signs of cell death, thus, indicated that DRO NPs has a significant killing effect on 4T1 tumor cells through PTT.

Study for DRO NPs reprogramming M2-like macrophages to M1-like phenotype, the RAW264.7 cells were treated with PBS, DA-

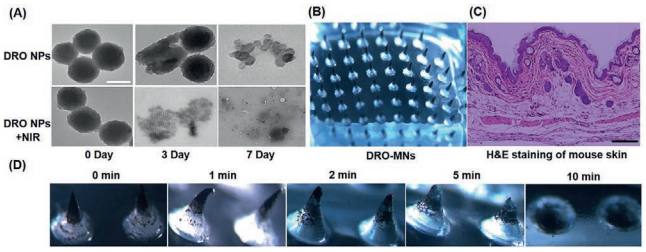


Fig. 4. The preparation and characterization of the soluble DRO-MNs. (A) The degrading characteristics of DRO NPs. Scale bar: 100 nm. (B) The appearance observation results of DRO-MNs through a microscope. (C) The H&E staining after inserting a DRO-MNs into mouse skin. Scale bar: 10 μm. (D) The photograph for recording dissolution of the DRO-MNs at different time points.

OVA NPs, DR NPs, and DRO NPs for 24 h. The expressions level of M1- and M2-related markers were then investigated using flow cytometry. The protein expressions of CD206 (M2-related marker) and CD197 (M1-related marker) in RAW264.7 cells were evaluated to assess the ability of DRO NPs to induce macrophage polarization. The results are shown in Fig. S2 (Supporting information). The DRO NPs group showed low expression levels of CD206 (approximately 25.43 %), similar to the DR NPs group (about 27.38 %). The DA-OVA NPs group (about 32.77 %) and the blank group (about 33.03 %) had higher expression levels (Fig. S3 in Supporting information). The expression ratio of CD197 in RAW264.7 cells was 28.47 % in the blank group, with slight increases in the DA-OVA NPs (36.28 %) and DR NPs (37.59 %) groups. In contrast, the CD197 expression ratio in the DRO NPs group was 59.37 %, significantly higher than in the other three groups. This finding indicates that DRO NPs effectively induce macrophage polarization towards the M1-type. Simultaneously, we also detected the expression of CD206 in RAW264.7 cells, which exhibited an opposite trend to CD197 (Fig. S4 in Supporting information). This result suggests that the number of M2 macrophages gradually decreases with DRO NPs treatment [31,32].

In vitro, the activation of DCs is indicated by the expression levels of CD80 and CD83 on DC2.4 cells. Flow cytometry was employed to detect the promotion of DCs cell maturation by DRO NPs in the DC2.4 cell line, using CD80 and CD83 as evaluation indicators for DCs maturation. The results are shown in Fig. S5 (Supporting information), where the expression of CD80 and CD83 increased in the DRO NPs group. The measurement value of CD80 was 13.79 %, which is twice that of the blank group (about 5.66 %), while the measurement value of CD83 was 8.54 %, five times greater than the blank group (1.45 %). Therefore, it can be concluded that DRO NPs significantly promote the maturation of DCs (Figs. S6 and S7 in Supporting information). The DRO NPs could activate APCs such as DCs, serving as an efficient adjuvant to stimulate the maturation of DCs and facilitate subsequent immune responses. In summary, DRO NPs can effectively activate DC2.4 *in vitro* [33,34].

Before preparing the DRO-MNs, we prepared DRO NPs with a particle size of 220 nm firstly, and the degradation of NPs under photothermal action was investigated. As shown in Fig. 4A, DRO NPs were placed in PBS *in vitro* for 7 days, and their degradation ability was determined using transmission electron microscope (TEM), without NIR, the complete NP profile can still be observed after 3 days, indicated that DRO NPs degrades slowly without NIR. NP fragments were still visible after 7 days, but the structure of DRO NPs start to collapse after 3 days under NIR, and most NPs were observed to have degraded on the seventh day. Then thoroughly mixed them with the constituent materials of the needle body to create a MN loaded with DRO NPs, this design allows for direct action on the tumor site while avoiding the side effects associated with systemic administration. The needle body of MN loaded with DRO NPs appears black-brown (Fig. 4B). In contrast, the needle body of the MN without DRO NPs is transparent white (Fig. S8 in Supporting information). After inserting the DRO-MNs into mouse skin, the skin was separated, and hematoxylin and eosin (H&E) staining was performed on its cut surface, the outline of the MNs can be seen in the mouse skin, indicating that the DRO-MNs possesses sufficient hardness to penetrate the skin smoothly and achieve transdermal drug delivery (Fig. 4C), this method can be employed for *in vitro* drug delivery in tumor-bearing mice. Furthermore, the dissolution of the soluble DRO-MNs was investigated, the MN gradually dissolved, and after about 10 min, it was completely dissolved (Fig. 4D), this result indicates that the DRO-MNs can quickly dissolve and release DRO NPs after penetrating the skin, thereby achieving therapeutic purposes [35].

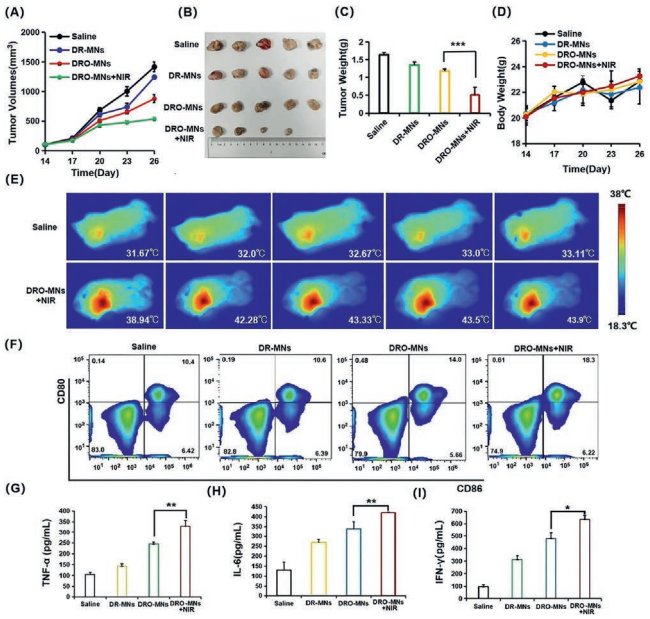


Fig. 5. Therapeutic efficacy and immunological evaluation of DRO-MNs in a 4T1 tumor model. (A) Average tumor growth kinetics after treatment. (B) Digital photographs of final tumor tissue after treatment with different formulations. (C) Average tumor weights at day 26 post-treatment. (D) Body weight curves of tumor-bearing mice after treatment with different formulations. (E) *In vivo* photothermal images of tumor-bearing mice after treatment with DRO-MNs+NIR, and saline group was as control. (F) Representative flow cytometry data to show DCs maturation induced by different formulations of MNs *in vivo*. (G–I) TNF-α, IL-6 and IFN-γ production in sera of tumor-bearing mice ($n = 3$), the data are shown as mean ± SD ($n = 5$). $^{*}P < 0.05$, $^{**}P < 0.01$, $^{***}P < 0.001$.

When the tumor volume of the tumor-bearing mice reaches about 100 mm^3, these mice were subjected to intratumoral treatments with saline, DR-MNs, DRO-MNs and DRO-MNs+NIR (R848, 2 mg/kg), administered on days 14, 17, 20, 23, and 26 to evaluate anti-tumor efficacy. All animal experiments were performed under the protocol approved by the Institutional Animal Care and Use Committee, Sun Yat-sen University (approval No. SYSU-IACUC-2024–001399). The tumor volume in the saline group grew rapidly, with its volume increasing approximately 13.74-fold compared to day 1 (Figs. 5A and B), and the tumor volumes in the DRO-MNs and DR-MNs groups increased ~12.63- and 9.58-fold, respectively, compared to day 1, the relatively slower growth of tumors in the DRO-MNs and DR-MNs groups may be attributed to immune enhancement in these groups. In contrast, the increase in relative tumor volume in the DRO-MNs+NIR group (~5.58-fold) was significantly lower than that in the DRO-MNs and DR-MNs groups. The DRO-MNs+NIR group exhibited a powerful tumor-suppressing effect compared to the saline group, with a reduction of about 2.64-fold. Mice treated with DRO-MNs+NIR exhibited the lowest tumor weight (0.5 ± 0.21 g), followed by the DRO-MNs (1.18 ± 0.05 g) and DR-MNs groups (1.35 ± 0.08 g, $P < 0.001$). These weights were no-

tably lower than those of the saline group (1.64 ± 0.05 g) (Fig. 5C). Although all groups of mice gained weight, there were no significant differences in body weight between them (Fig. 5D). Infrared thermal imaging is employed for evaluate the photothermal effect of DRO-MNs *in vivo*. In the DRO-MNs+NIR group, the temperature at the tumor site rapidly increased from 38.94 °C to 48.9 °C, while in the saline group, the temperature changed minimally, from 31.67 °C to 33.11 °C. These results suggest that DRO-MNs exhibit strong photothermal effects under 808 nm laser irradiation (Fig. 5E).

In addition, Ki-67 expression in tumor tissues was observed by immuno- fluorescence imaging. The increase in green fluorescence intensity caused by Ki-67 expression indicates the proliferation of 4T1 tumor cells in tumor tissue. The result was shown in Fig. S9 (Supporting information), the expression level of the Ki-67 marker is highest in the saline and DR-MNs groups, followed by the DRO-MNs and DRO-MNs+NIR groups. Notably, tumors treated with DRO-MNs+NIR showed the lowest expression of Ki-67 markers, indicating the formulation shows the strongest cytotoxic ability. TUNEL staining is also visualized through immunofluorescence imaging, where the intensity of green fluorescence produced by DNA fragmentation indicates damage to 4T1 cells in the tumor. Compared with other treatment groups, the DRO-MNs+NIR group exhibited the highest rate of apoptosis and the most pronounced inhibition of tumor cell proliferation. Additionally, as shown in H&E slices, most tumor cells were severely damaged in the DRO-MNs+NIR group, with significantly more destroyed tumor cells compared to the other groups. We conclude that DRO-MNs+NIR can strongly inhibit tumor growth and recurrence because they can effectively induce tumor necrosis and apoptosis through synergistic photothermal effects.

DRO-MNs exhibit robust immune responses *in vivo*, consistent with *in vitro* results, compared to the saline or DR-MNs group, the DRO-MNs group detected the highest CD86 and CD80 expression levels in the inguinal lymph nodes (LNs) of mice in this group on day 3 after immunization. The efficiency of DCs maturation was assessed using CD80 as a marker, it is well known that the upregulation of co-stimulatory molecules CD80 on the cell surface indicates the maturation of DCs, the role of DRO-MNs in DCs maturation and cross- presentation was evaluated. Notably, compared to the DCs maturation levels achieved by DR-MNs and DRO-MNs, the DRO-MNs+NIR group induced a higher level of DCs maturation, possibly due to the photothermal effect of DA NPs, which may induce ICD effects, further promoting DCs maturation (Fig. 5F). These results indicate that DRO-MNs+NIR could effectively activate DCs *in vivo* [36]. Conversely, CD86 (M1-type tumor-associated macrophages (TAMs) marker) was upregulated in the DR-MNs test groups compared to the saline group. Consequently, the DRO-MNs+NIR group exhibited a higher ratio of M1-type macrophages than the DR-MNs and DRO-MNs groups, suggesting that the final formulations can convert TAMs phenotypes due to the photothermal effect of the nano-system.

Polarized TAMs into M1-type phenotype and facilitating DCs maturation contribute to anti-tumor activity through cytotoxic T lymphocytes in the tumor microenvironment. Consequently, the expression of $CD4^+$ T and $CD8^+$ T cells in tumor tissue was evaluated by immunofluorescence labeling. The results showed that the infiltration degree of $CD4^+$ T and $CD8^+$ T lymphocytes in tumors was greatest in mice treated with DRO-MNs+NIR, as evidenced by the green fluorescence in the tumor sections, indicating maximal infiltration of T cells into the tumor microenvironment. Furthermore, immunofluorescence analysis of interferon-γ (IFN-γ) in tumor tissue administered with different formulations revealed that DRO-MNs+NIR treatment group significantly increased IFN-γ levels compared to the saline, DR-MNs, and DRO-MNs treatment groups. This suggests that activated $CD4^+$ T cells and $CD8^+$T cells within LNs may migrate into tumors, leading to substantial tumor suppression. The T cells in the DRO-MNs+NIR group exhibited expansion, regeneration, and differentiation capacities, generating terminally differentiated T cells with increased cytotoxicity (Fig. S10 in Supporting information). The results showed that DRO-MNs+NIR increased the infiltration of M1 macrophages and T lymphocytes into tumor tissue, which may enhance the anti-tumor effect related to the tumor microenvironment [37,38].

Cytokine secretion plays a crucial role in improving cellular immune response, therefore, measure the levels of cytokines such as TNF-α, IL-6 and IFN-γ in mouse serum indirectly evaluates the anti-tumor effect of MNs. In the DRO-MNs+NIR treated groups, elevated concentrations of TNF-α, IL-6 and IFN-γ were noted in the serum compared to the saline and DR-MNs groups, measuring 634.83 ± 31.8 and 419.78 ± 2.75 pg/mL, respectively (Figs. 5G and H). Additionally, IFN-γ levels in the DRO-MNs+NIR-treated group increased to 330.02 ± 27.38 pg/mL compared to the DRO-MNs-treated groups (Fig. 5I). In contrast, IL-10 secretion in serum significantly decreased after DRO-MNs+NIR treatment compared to saline and other treatment groups (Fig. S11 in Supporting information). The enzyme-linked immunosorbent assay (ELISA) analysis results indicated activation of the immune-suppressive in tumor microenvironment following formulation treatments. These results further confirm that the combined application of R848 and OVA, along with the NP photothermal effect, is related to the status of TAMs and $CD8^+$ T cells, it indicates that polarized TAMs as M1-type macrophages can enhance $CD8^+$ T cell function, ultimately leading to improved immunotherapy effects in tumor-bearing mice [39,40].

The therapeutic safety of DRO-MNs was evaluated by H&E staining on major organs such as the heart, liver, spleen, lungs, and kidneys of tumor bearing mice in each group, the result was as shown in Fig. S12 (Supporting information). No metastatic lesion was emerged in the liver and lung tissues of tumor-bearing mice in any group. Furthermore, no significant histopathological necrosis or inflammatory lesion was found at different time points following DRO-MNs therapy, and no lesion was detected in the heart, spleen, or kidney tissues. These results demonstrate the high safety and biocompatibility of the DRO-MNs in tumor therapy, providing a favorable guarantee for effective tumor treatment.

This study successfully established the transdermal delivery of R848 and OVA to tumor tissues using dissolvable DRO-MNs. The MN system demonstrated rapid dissolution in the tumor microenvironment, releasing DRO NPs that underwent efficient NIR-triggered biodegradation, enabling controlled and sustained drug release. The DRO-MNs achieved deep intratumoral penetration and maintained therapeutic efficacy for up to 72 h. Notably, the R848/OVA combination therapy effectively polarized TAMs and activated DCs, thereby overcoming tumor immunosuppression and potentiating systemic antitumor immunity. Moreover, the photothermal conversion capability of PDA NPs provided synergistic enhancement of immunotherapeutic outcomes. Importantly, the mechanical properties of these MNs are tunable through material composition, allowing for targeted drug delivery across various pathological conditions. Collectively, these results demonstrate the robust clinical potential of DRO-MNs as a versatile platform technology in precision cancer immunotherapy.

CRediT authorship contribution statement

Ping Sun: Writing – original draft, Methodology, Investigation, Formal analysis, Data curation. **Nansha Gao:** Writing – original draft, Methodology, Investigation, Data curation. **Li Yang:** Writing – original draft, Methodology, Investigation, Data curation. **Yao Yang:** Writing – original draft, Methodology, Investigation, Data curation. **Li Huang:** Methodology, Formal analysis, Data curation.

Hongzhong Chen: Methodology, Formal analysis, Data curation. **Hualin Ma:** Writing – review & editing, Supervision, Resources, Formal analysis. **Xiaowei Zeng:** Writing – review & editing, Supervision, Resources, Funding acquisition, Formal analysis, Conceptualization.

Declaration of competing interest

The authors declare that they have no known competing financial interests or personal relationships that could have appeared to influence the work reported in this paper.

Acknowledgments

We are grateful for the financial support from the Natural Science Foundation of Guangdong Province (No. 2023A1515110898), the Shenzhen Science and Technology Program (Nos. JCYJ 20230807093808018, JCYJ20220818102810023, JCYJ20230807112359022 and JCYJ20240813104000001), the University-Level Research Project of Guangzhou Vocational University of Science and Technology (No. 2025LG07), the Medical research Fund of Shenzhen Medical Academy of Research and Translation (No. C2301004), and the Shenzhen Fund for Guangdong Provincial High-level Clinical Key Specialties (No. SZGSP001).

Supplementary materials

Supplementary material associated with this article can be found, in the online version, at doi:10.1016/j.cclet.2025.112071.

References

[1] Y. Chen, J. Zhu, J. Ding, W. Zhou, Chin. Chem. Lett. 35 (2024) 108706.
[2] S.K. Roy, K.A. Ali, M. Biswas, et al., Curr. Drug Deliv. 22 (2024) 878–894.
[3] T.M. Tuan-Mahmood, M.T. McCrudden, B.M. Torrisi, et al., Eur. J. Pharm. Sci. 50 (2013) 623–637.
[4] T.T. Nguyen, Y. Oh, Y. Kim, et al., Hum. Vaccines Immunother. 17 (2021) 316–327.
[5] Y. Li, J. Yang, Y. Zheng, et al., Acta Biomater. 121 (2021) 349–358.
[6] T.T. Nguyen, J.H. Park, Expert Opin. Drug Deliv. 15 (2018) 235–245.
[7] J.L. Paris, L.K. Vora, M.J. Torres, et al., Drug Discov. Today 28 (2023) 103556.
[8] X. Jiang, S. Wang, L. Zhang, et al., Chin. Chem. Lett. 35 (2024) 108686.
[9] C. Liu, C. Han, J. Liu, Oncol. Res. 27 (2019) 965.
[10] T. Nie, Y. Fang, R. Zhang, et al., Bioact. Mater. 47 (2025) 51–63.
[11] S. Han, J. Wu, Bioact. Mater. 17 (2022) 300–319.
[12] J.Q. Wang, L.Y. Wang, S.J. Li, et al., Nanoscale 12 (2020) 15767–15774.
[13] B. Bahmani, H. Gong, B.T. Luk, et al., Nat. Commun. 12 (2021) 1999.
[14] K.A. Michaelis, M.A. Norgard, X. Zhu, et al., Nat. Commun. 10 (2019) 4682.
[15] M. Schön, M. Schön, Oncogene 27 (2008) 190–199.
[16] P. Zhou, J. Qin, C. Zhou, et al., Biomaterials 195 (2019) 86–99.
[17] E.J. Cheadle, G. Lipowska-Bhalla, S.J. Dovedi, et al., Leukemia 31 (2017) 1611–1621.
[18] J. Domingo-Diez, L. Souiade, V. Manzaneda-González, et al., Int. J. Mol. Sci. 24 (2023) 13306.
[19] X. Yan, K. Li, T.Q. Xie, et al., Angew. Chem. Int. Ed. 63 (2024) e202318539.
[20] G. Chen, Z. Yang, X. Yu, et al., J. Colloid Interface Sci. 652 (2023) 1108–1116.
[21] C. Ni, J. Lu, Z. Chen, et al., Mater. Des. 229 (2023) 111858.
[22] J. Li, L. Xie, B. Li, et al., Adv. Mater. 33 (2021) 2008481.
[23] J. Zhou, W. Zhao, Z. Miao, et al., ACS Nano 14 (2020) 2126–2136.
[24] L. Zhang, Y. Zhang, Y. Xue, et al., Adv. Mater. 31 (2019) 1805936.
[25] T. Zhao, L. Chen, M. Liu, et al., Nat. Chem. 15 (2023) 832–840.
[26] H. Guan, Z. Xu, G. Du, et al., Mater. Today Bio 19 (2023) 100610.
[27] P. Yang, S. Zhang, N. Zhang, et al., ACS Appl. Mater. Interfaces 11 (2019) 42671–42679.
[28] S. Huo, Z. Lyu, X. Wang, et al., Biomaterials 312 (2025) 122739.
[29] Y. Liu, C. Wang, S. Liu, et al., Int. J. Nanomed. 19 (2024) 10819–10837.
[30] H. Yuan, H. Gui, S. Chen, et al., Int. J. Nanomed. 19 (2024) 3589–3605.
[31] Y. He, L. Zhan, J. Shi, et al., Adv. Sci. 10 (2023) 2207650.
[32] X. Zhang, L. Yue, L. Cao, et al., Acta Biomater. 186 (2024) 369–382.
[33] L. Tian, Z. Tan, Y. Yang, et al., Acta Biomater. 169 (2023) 209–227.
[34] Z. Dong, W. Yang, Y. Zhang, et al., J. Control. Release 373 (2024) 172–188.
[35] S. Chen, J. Wang, L. Sun, et al., Biomaterials 311 (2024) 122687.
[36] H. Zhao, J. Xu, Y. Li, et al., ACS Nano 13 (2019) 13127–13135.
[37] B.T.N. Dang, R. Duwa, S. Lee, et al., J. Control. Release 372 (2024) 587–608.
[38] P. Sun, Z. Li, D. Zhang, et al., Chin. Chem. Lett. 35 (2024) 108346.
[39] H. Wu, G. Cao, M. Liu, et al., Chin. Chem. Lett. 36 (2024) 110493.
[40] F. Peng, Y. Xiang, H. Wang, et al., Small 18 (2022) 2204011.